Low-energy orbital excitations in strained $LaCoO_3$ films

Ru-Pan Wang,[1] Jaap Geessinck,[2] Hebatalla Elnaggar,[1] Yorick A. Birkhölzer,[2] Keisuke Tomiyasu,[3,4] Jun Okamoto,[5] Boyang Liu,[1] Chao-Hung Du,[6] Di-Jing Huang,[5] Gertjan Koster,[2] and Frank M. F. de Groot[1,*]

[1]*Debye Institute for Nanomaterials Science, Utrecht University, Universiteitsweg 99, 3584 CG Utrecht, The Netherlands*

[2]*MESA+ Institute for Nanotechnology, University of Twente, 7500 AE Enschede, Netherlands*

[3]*Department of Physics, Tohoku University, Aoba, Sendai 980-8578, Japan*

[4]*NISSAN ARC, LTD., 1, Natsushima-cho, Yokosuka, Kanagawa 237-0061, Japan*

[5]*Condensed Matter Physics Group, National Synchrotron Radiation Research Center, 101 Hsin-Ann Rd., Hsinchu Science Park, Hsinchu 30076, Taiwan, Republic of China*

[6]*Department of Physics, Tamkang University, 151 Yingzhuan Rd., Tamsui Dist., New Taipei City 25137, Taiwan, Republic of China*

(Received 2 October 2018; revised manuscript received 27 September 2019; published 31 October 2019)

We present 90 meV resolved Co $2p3d$ resonant inelastic x-ray scattering linear dichroism spectra of strained $LaCoO_3$ films and a $LaCoO_3$ single crystal. A polarization-dependent low-energy excitation is observed at ~0.2 eV on the tensile-strained $LaCoO_3/SrTiO_3$ film, while it is not observed in either bulk $LaCoO_3$ or the compressive-strained $LaCoO_3/LaAlO_3$ film. Guided by cluster calculations, we are able to distinguish the spin-state manifolds close to their transition point of Co^{3+} ions in $LaCoO_3$ systems. Through a polarization analysis, we show that the spin state can easily flip from a low-spin $^1A_{1g}$ state in an octahedral symmetry to the high-spin $^5B_{2g}$ or ^5E_g states with a small tetragonal distortion. A mixture of spin states suggests that the high-spin Co^{3+} plays an important role in long-range ferromagnetic order on both tensile- and compressive-strained $LaCoO_3$ films.

DOI: 10.1103/PhysRevB.100.165148

I. INTRODUCTION

The interaction between the charge, orbital, and spin is important in strongly correlated systems and as such they determine the physical properties of the $3d$ transition metal oxides. An example of a metal oxide with complex magnetic behavior is the perovskite $LaCoO_3$. A diamagnetic to paramagnetic transition at ~100 K has been observed in bulk $LaCoO_3$ and discussed as a spin crossover from a low-spin state (LS, $S = 0$) to a high-spin state (HS, $S = 2$) or, alternatively, to an intermediate-spin state (IS, $S = 1$) [1–6]. Long-range ferromagnetic order has been observed in epitaxially strained $LaCoO_3$ thin films [7–11], which implies that these $LaCoO_3$ thin films are ferromagnetic insulators for potential application in spintronic devices and therefore of technological relevance [12,13].

The ferromagnetic order in $LaCoO_3$ films is still under debate. It was initially described as being caused by the exchange interaction between LS and HS Co^{3+} ions [7–10]. Fuchs *et al.* proposed that the ferromagnetism of the $LaCoO_3$ thin films is caused by the Co-O-Co bond angle change because no bond length difference has been found from extended x-ray absorption fine structure (EXAFS) measurements [7,8]. The tetragonal distortion bends the Co-O-Co bond angle from ~163° to 180° and increases the superexchange interaction ($2J_{ex}$). Yet another EXAFS study observed the difference between in-plane and out-of-plane bond lengths [14]. This suggests that the octahedron deformation must be considered together with the octahedron rotation [15]. A tetragonal distortion breaks the ground-state symmetry and causes a competition between LS and HS Co^{3+} ions [14,16–18], as illustrated in Figs. 1(a)–1(d). Another explanation for the ferromagnetic ordering in films was proposed by Fumega and Pardo, where they suggested the presence of ordered oxygen vacancies (i.e., Co^{2+} ions), which in turn stabilize the ferromagnetic ordering [19,20]. This would imply that Co^{2+} ions are involved in a double-exchange-type interaction between Co^{3+} and Co^{2+}. However, experimental proof of the presence of Co^{2+} ions has not been established. On one hand, the existence of Co^{2+} ions is consistent with the experimental observation that the magnetic moment of $LaCoO_3$ film increases with thickness [18,21–23]. On the other hand, transmission electron microscopy (TEM) studies of structural defects do not provide a conclusive answer regarding the presence of oxygen vacancies as the results could be interpreted as both HS Co^{3+} or Co^{2+} [23–25]. Furthermore, x-ray absorption spectroscopy (XAS) and electron energy loss spectroscopy (EELS) measurements do not find large Co^{2+} concentrations in $LaCoO_3$ films. We point out as well that it has been found that a large amount of oxygen vacancies (>10%) strongly reduces the magnetism [13].

In an effort to contribute to the debate about the origin of magnetism in $LaCoO_3$, we employ $2p3d$ resonant inelastic x-ray scattering ($2p3d$ RIXS) to study the complex electronic configuration of the Co ions in a $LaCoO_3$ single crystal and strained thin films. $2p3d$ RIXS probes both the local [26–34] and collective excitations [35–42], including small lattice distortions [43–45]. In the case of $LaCoO_3$, the $2p3d$ RIXS process in the ionic limit can be described as $3d^6 > 2p^5 3d^7 > 3d^6$ transitions of Co^{3+} ions, which allows us to distinguish the spin-state manifolds. A bulk $LaCoO_3$ system

*F.M.F.deGroot@uu.nl

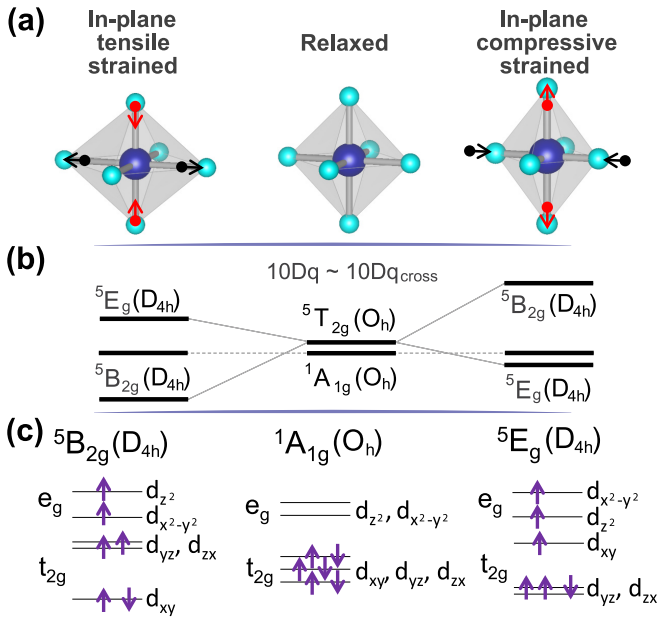

FIG. 1. (a) Octahedral oxygen network surrounding Co in relaxed and with in-plane compressive/tensile tetragonal distortions. (b) The splittings of the $^5T_{2g}(O_h)$ state in the tetragonal distortions. (c) Electronic configurations for the three ground states $^1A_{1g}(O_h)$, $^5B_{2g}(D_{4h})$, and $^5E_g(D_{4h})$.

(with Co in an octahedral oxygen network) has a LS $^1A_{1g}(O_h)$ ground state at low temperature, whereas small tetragonal distortion causes a ground-state change when the crystal-field energy (10Dq) is close to the crossover point (10Dq$_{cross}$), as demonstrated in Fig. 1(b). The three possible electronic configurations in tetragonal (D_{4h}) symmetry are, respectively, $^1A_{1g}$, $^5B_{2g}$, and ^5E_g [Fig. 1(c)]. RIXS measurements on the single crystal $LaCoO_3$ indicate that the spin-state population is varying as a function of temperature, which suggests that the ground state is close to a degeneracy of LS $^1A_{1g}(O_h)$ and HS $^5T_{2g}(O_h)$ states [42,46]. Furthermore, different composition mixtures of LS and HS states have been found in the cuboidal (D_{2h}) and trigonal (D_{3d}) distorted $LaCoO_3$ films through $2p3d$ RIXS [45], which agrees with x-ray diffraction [10].

In this paper, incident photon polarization analysis is presented to gain deeper insight into the electronic configurations. Guided by simulations, a unit cell volume-conserving model provides a systematic approach to discuss the strain effects. The observed RIXS features can be identified using a polarization-dependent analysis. We show that the dichroism intensities are related to the ground-state symmetries and change as a function of the distortion parameters from a tensile- to a compressive-strained $LaCoO_3$.

II. METHOD

A. Sample preparation and characterization

The distortion effect of $LaCoO_3$ was studied on three different samples: an unstrained $LaCoO_3$ single crystal, a tensile-strained $LaCoO_3$ film on (001)-$SrTiO_3$, and a compressive-strained $LaCoO_3$ film on (001)-$LaAlO_3$. The $LaCoO_3$ single crystal was grown in O_2 gas flow by the floating-zone method at the department of physics in Tohoku University. It was prepared from a polycrystalline sample obtained by a stoichiometric mixture of high-purity powders of La_2O_3 and Co_3O_4 as described in the Supplemental Material of Ref. [46]. The $LaCoO_3$ thin films were fabricated at the MESA+ Institute of the University of Twente using pulsed laser deposition combined with *in situ* reflection high-energy electron diffraction to monitor the growth process. The films were grown under a 0.2 mbar O_2 background pressure and at a deposition temperature of 750 °C and a laser fluence of 1.9 J/cm^2. 55 nm $LaCoO_3$ films were prepared on, respectively, (001)-$SrTiO_3$ and (001)-$LaAlO_3$ substrates, where the layer thickness was determined by x-ray reflectivity.

TABLE I. The lattice constants as obtained from x-ray diffraction (length in Å). V refers to the calculated volume of the pseudocubic unit cell.

	Substrate	$LaCoO_3$(**a**)	$LaCoO_3$(**c**)	V	ϵ
Crystal	–	3.83		56.2	–
On $SrTiO_3$	3.91		3.78	57.8	2%
On $LaAlO_3$	3.79		3.84	55.2	−1%

The lattice constants were determined by the x-ray diffractions measured along the (00ℓ) orientation and by the reciprocal space maps on the (103) feature, from which the out-of-plane and in-plane lattice information could be obtained [Figs. 2(a)–2(c)]. High-resolution scans were performed in the triple axis configuration with a parabolic x-ray mirror, four-bounce Bartels monochromator, and Ge analyzer crystal on a PANalytical X'Pert Pro MRD system with a sealed tube Cu anode source in line-focus mode. The asymmetric reciprocal space maps were obtained from sets of high-resolution rocking curves collected with an EIGER2 R 500 K area detector on a Bruker D8 Discover diffractometer. High brilliance microfocus Cu rotating anode generator, Montel optics, and a Ge (220) two-bounce monochromator were used in these measurements. To determine the magnetic transition temperature of both films, field-cooled magnetization measurements were performed using vibrating sample magnetometry (VSM), see Fig. 2(d). Both the tensile- and compressive-strained $LaCoO_3$ films show in-plane ferromagnetism with an onset transition temperature of ∼70 K. The paramagnetic to diamagnetic transition of the $LaCoO_3$ single crystal occurs at ∼100 K [46].

Table I lists the lattice constants extracted from the diffraction results. The pseudocubic lattice constant of the single crystal $LaCoO_3$ $\mathbf{a_{cub}}$ ∼ 3.83 Å was obtained by projection from R$\bar{3}$C (012) to cubic (001) symmetry. This value shows good agreement with literature [7,8,47]. For the $LaCoO_3$ films, the out-of-plane lattice constants ($\mathbf{c_{LCO}}$) are ∼3.78 Å and ∼3.84 Å on the $SrTiO_3$ and $LaAlO_3$ substrates, respectively. We note that the absence of the Laue fringes in Fig. 2(a) might be due to the partial strain relaxation, the surface roughness, and/or the imperfect crystallinity of the films. In Fig. 2(a), more than one out-of-plane lattice parameter can also be observed (indicated by the stars) for the $LaCoO_3$ thin films, which implies the coexistence of strained and partially relaxed $LaCoO_3$ phases in the films. The volume proportions of the strained component were estimated to be

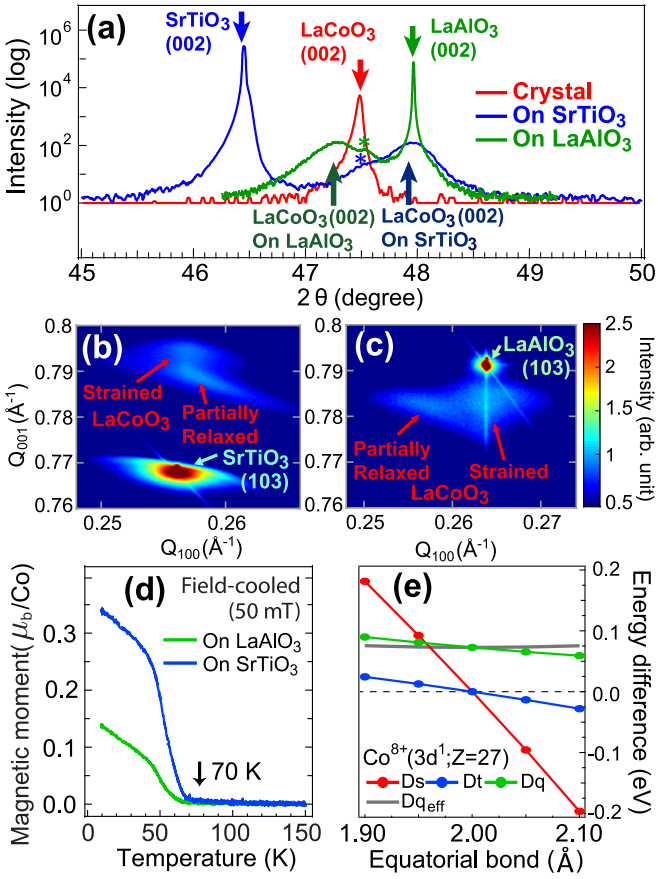

FIG. 2. (a) The x-ray diffraction patterns (θ-2θ scans) of the (002) feature of the $LaCoO_3$ single crystal and the 55 nm $LaCoO_3$ films. The red arrow is for the $LaCoO_3$ single crystal. The blue and green arrows indicate the substrate peaks of $SrTiO_3$ and $LaAlO_3$. The dark green and dark blue arrows indicate the (002) feature of $LaCoO_3$ films on the $LaAlO_3$ and $SrTiO_3$ substrates, respectively. The stars indicate the partially relaxed $LaCoO_3$ component in the films. (b), (c) The two-dimensional reciprocal space map of the (103) feature for (b) the $LaCoO_3/SrTiO_3$ film and (c) the $LaCoO_3/LaAlO_3$ film. (d) The in-plane field-cooled VSM measurement in 50 mT as a function of temperature. (e) The crystal-field parameters of the tetragonal distorted Co^{8+} ion, derived from a model calculation in a volume-conserving cluster.

~73% strained film on the $SrTiO_3$ substrate and ~90% on the $LaAlO_3$ substrate (see Appendix A). In other words, the majority of the film is strained coherently for both substrates, where we note that the values are model dependent with an uncertainty of ~10%. This coexistence between strained and partially relaxed fractions is also supported by the two-dimensional reciprocal space maps along the in-plane (Q_{100}) and the out-off-plane (Q_{001}) orientations. The strained fraction of the film has the same in-plane momentum as the substrate and can therefore be found vertically above [in the case of $SrTiO_3$, Fig. 2(b)] and below [in the case of $LaAlO_3$, Fig. 2(c)] the substrate peak in the reciprocal space maps. The match of the in-plane momentum magnitude implies that the in-plane lattice constants ($\mathbf{a_{LCO}}$) are identical to the lattice constants of the substrates, which are 3.91 Å and 3.79 Å for the films on $SrTiO_3$ and $LaAlO_3$ substrates, respectively. The partially relaxed fractions of the film are those that have a different in-plane momentum. Both thin films are in the elastic deformation limit ($-1\% < \epsilon < 2\%$), where ϵ is defined as $\epsilon = (\mathbf{a} - \mathbf{a_{cub}})/\mathbf{a_{cub}}$ [8,18,48–50]. The diffraction results also show that the difference in unit cell volume between the thin film samples and the single crystal is less than 3%, which implies that the unit cell volume is approximately conserved in the strained samples.

B. Simulation model

Cluster calculations were performed including charge transfer and tetragonal distortion using the program QUANTY. This program can solve the many-body problem, including configuration interactions [51–53]. The Hamiltonian of a single cluster is written as

$$H = H_{\text{ionic}} + V_{\text{CF}} + H_{\text{mix}}, \tag{1}$$

where H_{ionic} describes the intra-atomic interactions, such as the Coulomb interaction and the spin-orbit coupling. The operator H_{mix} calculates the interaction between the three configurations d^n, $d^{n+1}\underline{L}$, and $d^{n+2}\underline{L}^2$ using the single impurity Anderson model [51,54]. This configuration interaction mimics the charge transfer effect. The symmetry characteristic of the cluster is considered in the operator V_{CF}, which also determines the crystal-field energies. For tetragonal distorted clusters, the $3d$ orbitals split into the a_1, b_1, e, and b_2 states. The energy splitting of these states can be determined by the additional parameters Dt and Ds in comparison with the unstrained cubic crystal in the simulation [51]. It induces more degrees of freedom in the parameters to simulate the electronic structure.

To reduce the number of the parameters, we applied constraints by assuming that the local cluster preserves its volume. This assumption is based on the diffraction results, which indicate a <3% difference in volume (Table I) of the pseudocubic unit cell (CoO_6 cluster). Model calculations were performed using the program MULTIX [52], where the energy levels can be calculated with a spherical Wigner local density approximation atomic radial function in an electric field potential with point charges [52,53]. We simulated the distortion effect for the case of a single electron in a $3d$ shell ($3d^1$) by assuming that it is independent of the electron-electron interaction. In this model calculation, the metal-ligand bond (d) was set to 2 Å for a nondistorted cluster (d ~ 1.9 Å for $SrTiO_3$) [8]. The volume restriction is fixed at $d_x \times d_y \times d_z = 8$ Å^3, where d_x, d_y, and d_z are the bonds along the x, y, and z axes. Based on the values of the energy levels, the crystal-field parameters Dq, Ds, and Dt can be extracted [51]. We introduce an effective 10Dq ($10Dq_{\text{eff}}$) parameter, which is defined as the energy difference between the average energy of the e_g and t_{2g} states. The values of Dq, Dq_{eff}, Ds, and Dt of the model calculation are indicated in Fig. 2(e) as a function of the equatorial bond ($d_x = d_y$). The following conclusions can be drawn: (i) A negative Ds and Dt values are found for an elongated d_x related to the tensile-strained $LaCoO_3$ film on $SrTiO_3$. (ii) Comparing the values Dt and Ds, we find a Dt to Ds ratio ~0.15 for the Co ion. (iii) $10Dq_{\text{eff}}$ is approximately constant [gray lines, Fig. 2(e)]. In our simulation, we applied the optimized values of the Slater integrals and 10Dq

for the unstrained $LaCoO_3$ crystal [46], and used the unit cell volume-conserving approach for the films. This method allows us to investigate the distortion effect systematically varying only the Ds parameter.

C. The 2*p*3*d* RIXS experiment

The XAS and RIXS results were carried out at the 05A1 RIXS beamline in Taiwan Light Source, where the AGS-AGM system provides a 90 meV (in full width half maximum, FWHM) experimental RIXS resolution at the cobalt L_3 edge [55]. The incident photon energy broadening is determined by the gap of the slit after the monochromator. In the RIXS measurements, the value of slit gap was 100 μm, which provides an incident energy broadening ~1 eV (FWHM). Thanks to the energy compensation principle, the wide incident energy broadening will not change the experimental RIXS resolution [56]. Partial fluorescence yield XAS was also collected using a silicon photodiode to calibrate the incident photon energy. During XAS measurements, the incident photon energy resolution was ~0.6 eV FWHM (slit gap ~50 μm), which is smaller than the linewidth of the L_3 edge of $LaCoO_3$ [6]. All incident energies were identified with respect to the maximum of the L_3 edge. The precision of the energy calibration is not changed upon increasing the gap of the slit to obtain more flux in the RIXS experiment. The intensity of the RIXS spectra is influenced by the ion concentration, the exposed area of the sample, and the probing path, which implies that different samples cannot be directly compared to each other. To compare the spectra acquired from different samples in a consistent approach, we normalized the experimental spectra according to both the exposure time and the area of the fluorescence profile. Further details of the experiments can be found in the Supplemental Material of Ref. [42].

III. RESULTS AND DISCUSSIONS

A. Experimental results

Figure 3(a) compares the fluorescence yield XAS spectra acquired from two orthogonal linear polarized incident beams. The linear vertical (V) and horizontal (H) polarized beams are defined by the electric field orientation as illustrated in Fig. 3(b). During the measurements of the crystal and the films, the (001) and (010) orientations of the samples were placed in the scattering plane. The XAS results [Fig. 3(a)] show that the shoulder above the edge (at ~783.5 eV) is higher in the case of the $LaCoO_3$ single crystal, which can be attributed to the LS $^1A_{1g}(O_h)$ ground state [6,20]. The isotropic $^1A_{1g}(O_h)$ state also implies that there is no polarization dependence in the dipole transition, as confirmed by the overlap of the two polarization-dependent spectra. In addition, bulk sensitive fluorescence yield XAS spectra show no characteristic features of Co^{2+} ions [33,44].

The maximum of the Co L_3 edge [E_{in}, Fig. 3(a)] was selected for the RIXS measurements. The experiments were aligned at a grazing incident geometry ($\theta \sim 10^\circ$) with the spectrometer at 90°. Two types of features are identified from the results [Fig. 3(c)]: sharp excitonic peaks between 0 and 3 eV and the broad fluorescence feature above 3 eV. This broad feature was used for normalization purposes. At 20 K,

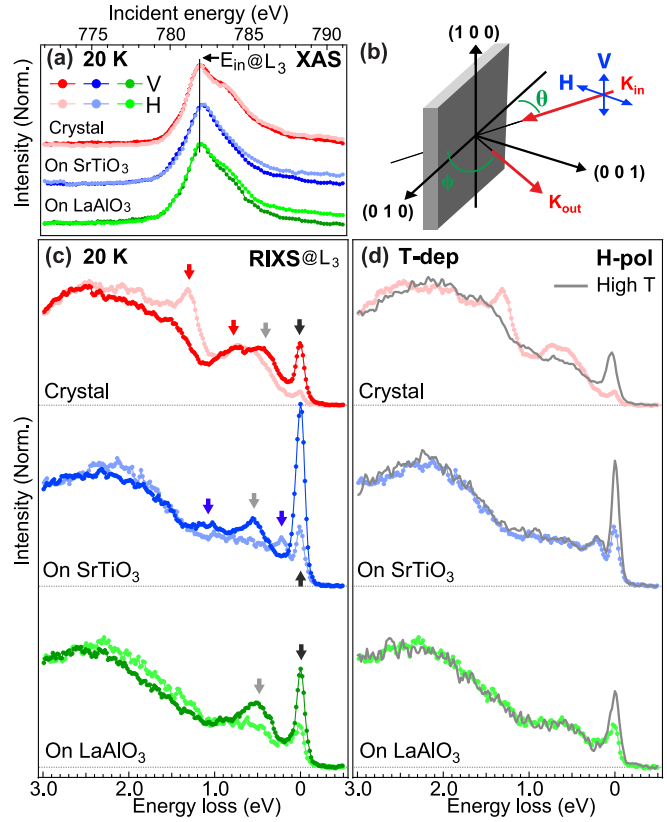

FIG. 3. (a) The fluorescence yield XAS results. E_{in} indicates the maximum of the L_3 feature for the RIXS measurement. (b) Illustration of the experimental geometry. (c) Polarized RIXS spectra at the L_3 edge for $LaCoO_3$ crystal and $LaCoO_3$ films. The dark and light color circles indicate the spectra of V- and H-polarization beams, respectively. The black, red, and blue arrows refer to the elastic peak, the characteristic features of $LaCoO_3$ single crystal, and the characteristic features of $LaCoO_3$ film on $SrTiO_3$ substrate, respectively. The gray arrows indicate the mixture of spin states. (d) The comparison of H-polarization spectra between low temperature (color) and high temperature (gray). The measurements are performed at a temperature 150 K for the films and 300 K for the single crystal.

the excitations of the $LaCoO_3$ single crystal are located at about 0, 0.4, 0.8, and 1.3 eV [arrows in Fig. 3(c)]. These features behave differently in the films. The 0.8 eV and 1.3 eV features (red arrows) become weaker or disappear in both films. In addition, the $LaCoO_3/SrTiO_3$ film [Fig. 3(c)] shows two extra features at 0.2 eV and 1.1 eV (blue arrows) while the $LaCoO_3$ crystal and the $LaCoO_3/LaAlO_3$ film do not exhibit these features. In particular, the 0.2 eV feature shows a strong polarization dependence. The feature marked with gray arrows in Fig. 3(c) might be the contribution of spin-state mixtures between HS and LS $LaCoO_3$, which will be discussed later.

Figure 3(d) compares the measurements below and above the magnetic transition temperature (~70 K). The high-temperature measurements were performed at 150 K for the films and at 300 K for the single crystal. The $LaCoO_3$ single-crystal RIXS spectra change with temperature due to the transition from a pure LS $^1A_{1g}(O_h)$ state to a mixture

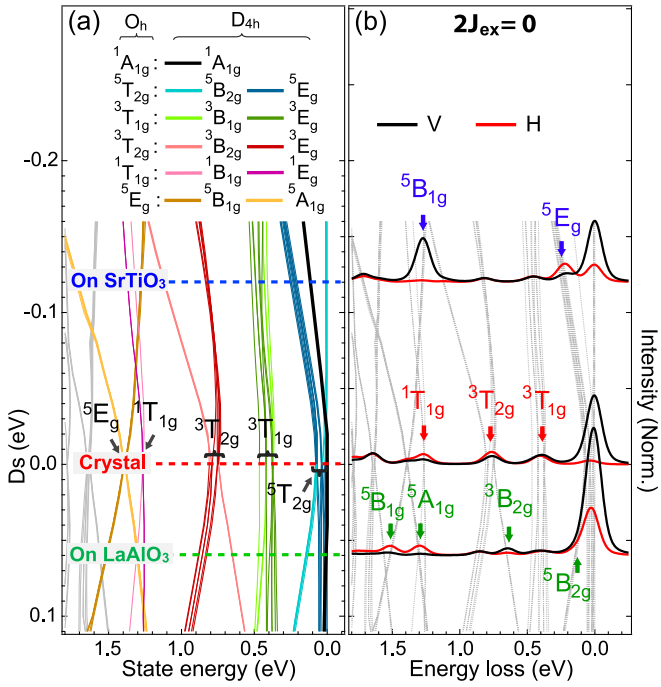

FIG. 4. The calculation of (a) the energy diagram and (b) the RIXS spectra as a function of the distortion parameter Ds. The red, blue, and green arrows refer to the characteristic features of the LS $^1A_{1g}(O_h)$, HS $^5B_{2g}(D_{4h})$, and HS $^5E_g(D_{4h})$ ground states, respectively. The incident energy was selected at the maximum of the L_3 feature.

between the LS $^1A_{1g}(O_h)$ and HS $^5T_{2g}(O_h)$ states. In contrast, in the strained $LaCoO_3$ films, no spectral difference is visible except for the elastic peak, implying that the spin state does not change in this temperature region. The elastic peak is enhanced because of the thermal population of lattice vibration excitations (<20 meV) [57,58] or the excitations from thermally excited states within the same $^5B_{2g}(D_{4h})/^5E_g(D_{4h})$ manifold (<50 meV) [46]. These quasielastic features cannot be distinguished due to the resolution limit. We point out that the experimental temperature difference between the single crystal and the films will not influence the discussion, because both the temperatures at 150 K and at 300 K are well above the crossover temperature of the single crystal (∼100 K). Tomiyasu *et al.* have shown that the HS $^5T_{2g}(O_h)$ state starts to dominate the contribution to the spectra of the single crystal above 150 K [46].

B. Distortion dependent calculations

Figure 4(a) presents the energy diagram as a function of the tetragonal distortion parameter Ds. The charge transfer parameters were implemented as follows: U = 6.5 eV, Q = 7.5 eV, $T_{t_{2g}} = 1.8$ eV, and $T_{e_g} = 3.118$ eV [46]. The intraatomic Slater integrals of the 3*d* states were 92.5% from the atomic values ($F^2_{dd} = 9.371$ eV and $F^4_{dd} = 5.859$ eV) and the 3*d* spin-orbit coupling was 55 meV. The charge transfer effect decreases the ionic 10Dq value to 0.595 eV. Figure 4(a) shows that the $^5B_{2g}(D_{4h})$ and $^5E_g(D_{4h})$ splitting of the $^5T_{2g}(O_h)$ excited state changes the ground state when the distortion is applied. The $^3T_{1g}(O_h)$ excited state splits into $^3E_g(D_{4h})$ and $^3B_{1g}(D_{4h})$ states. This $^3T_{1g}(O_h)$ excited state is located at about 0.4 eV and does not show strong tetragonal distortion dependence. In contrast, the $^3T_{2g}(O_h)$ excited state is more sensitive to the distortion effect and splits into $^3E_g(D_{4h})$ and $^3B_{2g}(D_{4h})$ states.

The Ds value for the $LaCoO_3/SrTiO_3$ film was determined to be ∼−0.12 eV, according to the 0.2 eV feature using the energy diagram [blue dashed line in Fig. 4(a)]. The Ds value for $LaCoO_3/LaAlO_3$ film was estimated at ∼0.06 eV (cf. Table I) using linear extrapolation. These values are slightly larger than the values estimated from our volume-conserving approach [Ds ∼0.04 eV for a 1% mismatch, cf Fig. 2(e)], which is partly caused by the symmetry breaking of the octahedral charge transfer. Considering the hopping parameters T_{a_1}, T_{b_1}, T_e, T_{b_2} (D_{4h}) instead of only using T_{e_g}, $T_{t_{2g}}$ (O_h) introduces an additional state splitting, which leads to larger Ds values. Figure 4(b) displays the calculation of the 2*p*3*d* RIXS spectra with respect to different distortion values. We applied 0.05 eV Lorentzian broadening convoluted with a 0.10 eV Gaussian broadening in FWHM to the final state energy. The broadening of the incident energy was simulated by a convoluted broadening of 0.3 eV Lorentzian broadening and 1.0 eV Gaussian broadening in FWHM to simulate the wide incident energy window of the AGM-AGS system. The calculated spectra in Fig. 4(b) have been performed at the maximum of the L_3 resonant edge of V-polarized incident beam and all the intensities were normalized to the total intensity of the charge-transfer features.

An important observation is that positive and negative Ds exhibit different polarization dependence for the excitons. In Fig. 4(b), the peak of zero energy loss indicates the transition back to the ground state. The features corresponding to the $^3T_{1g}(O_h)$, $^3T_{2g}(O_h)$, and $^1T_{1g}(O_h)$ excited states originating from an $^1A_{1g}(O_h)$ ground state can be observed (red arrows) with weak polarization dependence. For a $^5B_{2g}(D_{4h})$ ground state, the $^5E_g(D_{4h})$ excited state at ∼0.2 eV is enhanced by the H-polarized incident photon. Another noticeable feature is the $^5B_{1g}(D_{4h})$ excited state, which shows similar polarization selectivity as the $^5B_{2g}(D_{4h})$ ground state. In contrast, a $^5E_g(D_{4h})$ ground state shows a strong polarization dependence of the zero energy loss peak. Weak polarization dependence appears at ∼1.3 and ∼1.5 eV, related to the $^5A_{1g}(D_{4h})$ and $^5B_{1g}(D_{4h})$ excitations. The dichroic intensity of the $^3B_{1g}(D_{4h})/^3E_g(D_{4h})$ and $^3B_{2g}(D_{4h})/^3E_g(D_{4h})$ excitations are weak [Fig. 4(b)].

C. Comparison of L_3 edge results

The simulation in Fig. 4(b) overestimates the polarization dependence of the $^5B_{2g}(D_{4h})$ to $^5B_{1g}(D_{4h})$ excitation, which is likely related to a mixture of spin states. The spin-state mixture has been observed in the tensile D_{2h} and D_{3d} distorted $LaCoO_3$ and explained as the LS-HS spin state ordering [9,10,45]. Such frozen electron configuration provides long-range ferromagnetic order [9,10,59]. We note that we can identify the spin-state characteristics according to the polarization-dependent feature in the energy region between 0 and 500 meV, but the relatively high noise level of the RIXS spectra of the $LaCoO_3$ films makes a detailed quantitative interpretation difficult. According to the XRD results, the

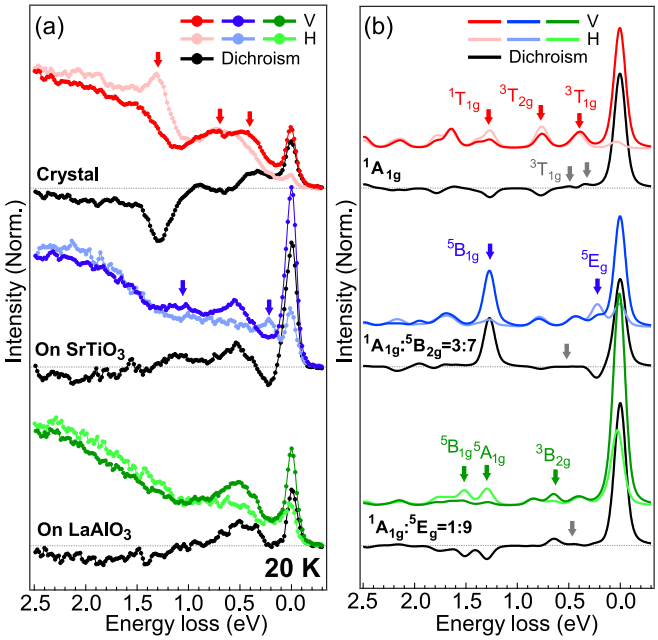

FIG. 5. The comparison of the dichroism spectra excited at E_{in}. (a) Experiment and (b) simulation. The red, blue, and green arrows refer to the characteristic features LS $^1A_{1g}(O_h)$, HS $^5B_{2g}(D_{4h})$ and HS $^5E_g(D_{4h})$ ground states, respectively. The gray arrows indicate the possible of spin state mixture as discussed in the text.

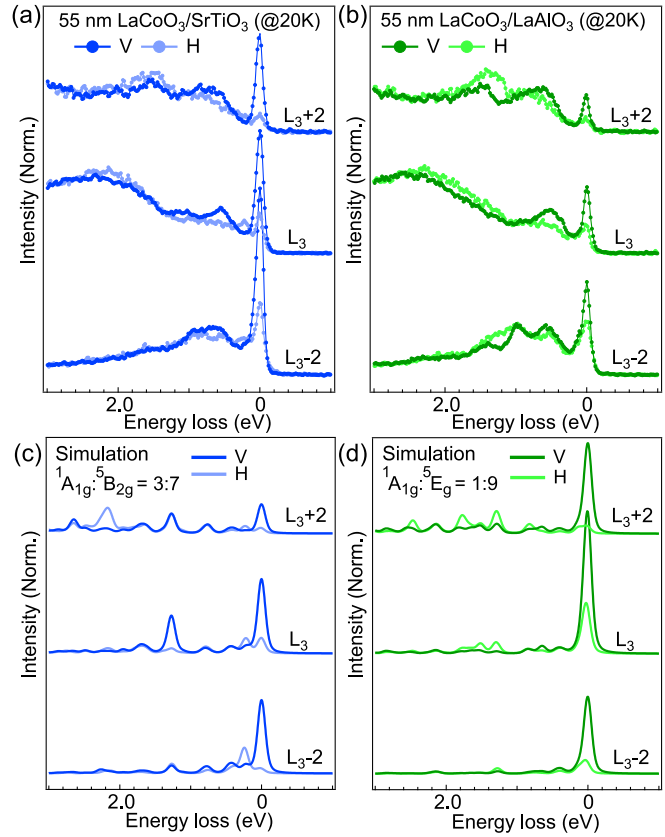

FIG. 6. (a), (b) The energy-dependent RIXS spectra of 55-nm $LaCoO_3$ films on the (a) $SrTiO_3$ substrate and (b) $LaAlO_3$ substrate. (c), (d) The simulation for the mixture of (c) $^1A_{1g}$ and $^5B_{2g}$ states and (d) $^1A_{1g}$ and ^5E_g states.

LS-HS spin-state ratio is approximately 3:7 (∼73% HS state) and 1:9 (∼90% HS state) for the tensile- and compressive-strained $LaCoO_3$ films, respectively.

Figure 5 compares the experimental dichroism spectra to the simulations. The spectra of the $LaCoO_3$ single crystal at 20 K can by simulated well by a pure $^1A_{1g}(O_h)$ state [6,45,46]. For the tensile-strained $LaCoO_3/SrTiO_3$ film, ∼70% of the $^5B_{2g}(D_{4h})$ state is included. The dichroism feature at ∼0.2 eV is reproduced, but the dichroism intensity of the $^5B_{1g}(D_{4h})$ state is larger in the calculations. Comparing the RIXS dichroism spectra on $LaCoO_3/LaAlO_3$ film, we observed no feature at about 0.2 eV, which is in agreement with the simulation. The intensity discrepancy on the $LaCoO_3/SrTiO_3$ film might be because of the fitting uncertainty of the XRD features, where the LS state population can be underestimated. By increasing the LS state population, the dichroism intensity of the $^5B_{1g}(D_{4h})$ state will be reduced and the dichroism intensity in the energy region between 0.2 and 1.0 eV (gray arrows) can also be improved.

The mixed spectrum shows better agreement, which implies the existence of spin-state mixtures and suggests that the HS Co^{3+} can be the trigger of long-range ferromagnetic order. Some other discrepancies remain related to the fact that (i) $10Dq_{eff}$ was constrained to a constant in all the cases, while the position of high-energy excitations are changed when different $10Dq_{eff}$ values are applied; (ii) although the $^1A_{1g}$ ground state does not split, the tetragonal symmetry splits the $^3T_{1g}(O_h)$ excited state into the $^3B_{1g}(D_{4h})$ and $^3E_g(D_{4h})$ states, which can yield different dichroism intensity with respect to the excitation in octahedral symmetry; (iii) the zero energy loss features are lower in the experiments than in the calculations due to the energy-dependent self-absorption effect, as discussed in Appendix B.

D. Energy-dependent RIXS spectra

Figure 6 shows the experimental and simulated spectra excited at L_3 edge and $L_3 \pm 2$ eV using the same theoretical models. The fine structures are more pronounced at L_3 −2 eV due to the suppressed fluorescence features experimentally [46], but the pre-edge RIXS spectrum is sensitive to the small resonant features which bias the adjustment of the energy in the simulation. These resonant features are hidden in the tail of the absorption maximum and modify the calculations. Such difficulty can also be found in the high-quality XAS results [6]. For better determination of the energies, to discuss more precise simulation parameters, a fine step energy map is required. In the Fig. 6(a), a feature at 0.2 eV appears which is always enhanced by the H-polarized incident photon. This observation agrees with the simulation results [Fig. 6(c)]. In addition, when we excite at the absorption maximum (L_3 edge), the feature of the $^5B_{1g}(D_{4h})$ excited state is enhanced by V-polarized incident photon and pronounced at about 1.1 eV in the experiment and 1.3 eV in the simulation. The energy discrepancy could be compensated by manipulating the $10Dq_{eff}$, which is constrained to a constant in our model. Whereas, the $LaCoO_3/LaAlO_3$ film [Fig. 6(b)] shows similar RIXS dichroism intensity of the 1.3 eV feature to the bulk

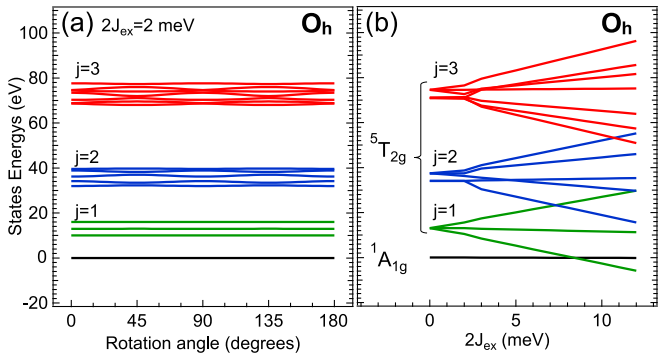

FIG. 7. (a) The energy diagram of $^1A_{1g}(O_h)$ and $^5T_{2g}(O_h)$ states as a function of $2J_{ex}$ rotation angle along z axis, where $|2J_{ex}|$ is fixed at 2 meV. (b) The energy diagram of $^1A_{1g}(O_h)$ and $^5T_{2g}(O_h)$ states as a function of $2J_{ex}$ value.

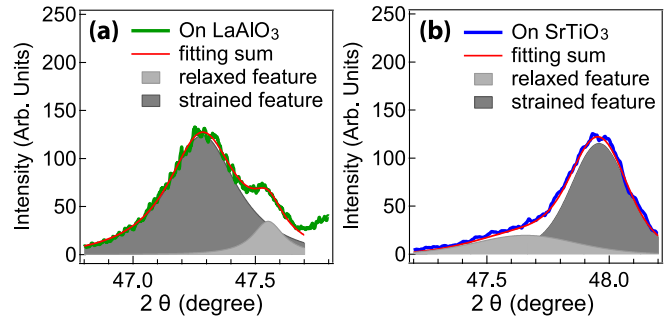

FIG. 8. Quantifications of the x-ray diffraction results for the $LaCoO_3$ films on the substrate (a) $LaAlO_3$ and (b) $SrTiO_3$.

sample but no feature at ∼0.2 eV. The presence of the 1.3 eV feature in the $LaCoO_3/LaAlO_3$ film might be contributed by two sources of $^1A_{1g}(O_h)$ ground state as well as $^5E_g(D_{4h})$ ground state. It suggests a mixture of spin states as previously discussed, which matches the simulation [Fig. 6(d)].

E. Effects of rotation

It has been suggested that the angle between two octahedra in the perovskite is important for the magnetic order [7,15]. We hereby investigate the octahedron rotation effect by off-aligning the direction of $2J_{ex}$. Figure 7(a) presents the energy diagram as a function of $2J_{ex}$ rotation angle along z axis, where $|2J_{ex}|$ is fixed at 2 meV. We find that the energy splitting is independent of the orientation of $2J_{ex}$ in our mean-field calculation. A way to change the ground-state symmetry is by increasing the value of $|2J_{ex}|$. Figure 7(b) indicates that for a change of the ground-state symmetry, a $|2J_{ex}|$ value larger than 8 meV is required. It suggests that another mechanism might be involved to enlarge the $|2J_{ex}|$ value, which is beyond the ability of our calculation treatment.

Although the octahedron rotation does not change the ground-state symmetry, the combined effect of octahedron rotation and octahedron deformation might reflect on the polarization dependence of the spectra. We show in the Appendices that the rotation mismatch will change the dichroism intensity [see Fig. 9(b)]. By including the off-aligned tetragonal field, both the elastic and the $^5B_{1g}$(∼1.3 eV) features decrease in intensity, which brings the simulated result of the $LaCoO_3/SrTiO_3$ film closer to the experiments.

IV. CONCLUSION

$2p3d$ RIXS dichroism spectra can be used to determine the nature of the ground state. A theoretical approach is proposed where a unit cell volume-conserving model reduces the parameters for systematic discussion. Using linear dichroism analysis, we show that the Co^{3+} ions are dominated by the $^1A_{1g}(O_h)$ state in a $LaCoO_3$ single crystal, whereas, the tensile- and compressive-strained $LaCoO_3$ films on $SrTiO_3$ and $LaAlO_3$ contain contributions from the $^5B_{2g}(D_{4h})$ and $^5E_g(D_{4h})$ states, respectively. A 0.2 eV excitation was observed in the tensile-strained $LaCoO_3/SrTiO_3$ film by $2p3d$ RIXS, which is attributed to an orbital excitation from the $^5B_{2g}(D_{4h})$ to the $^5E_g(D_{4h})$ state. No feature appeared at this energy region in the compressive-strained $LaCoO_3/LaAlO_3$ film. The spectra of the films show no temperature dependence, implying that the spin state does not change above the transition temperature (∼70 K). The composition mixture agrees with the existing picture of strain-induced differences, where we note that the discrepancies and the noise level of the dichroism intensity limit the quantitative interpretation. Bulk sensitive fluorescence yield XAS shows no Co^{2+} features, therefore the data suggests that the HS Co^{3+} can be the trigger of long-range ferromagnetic order due to the possible existence of quantum-chemical mixed spin states.

ACKNOWLEDGMENTS

The authors thank Yu-Hui Liang for supporting the x-ray diffraction measurements and Ties Haarman for providing the fitting codes for the RIXS spectra. We thank the technical staff of Taiwan Light Source for their help with RIXS measurements. The experiments were supported by an ERC advanced grant (Grant Agreement No. 340279-XRAYonACTIVE). D.-J.H. was supported by the Ministry of Science and Technology of Taiwan under Grant No. 106-2112-M-213-008-MY3. K.T. was financially supported by the MEXT and JSPS KAKENHI (No. JP17H06137, No. JP15H03692, No. JP18K03503). C.-H.D. was supported by the MOST through the Grant No. 105-2119-M-032-002-MY2. J.G. and G.K. acknowledge the Netherlands Organisation for Scientific Research (NWO) and the NWO/FOM programme DESCO (VP149).

APPENDIX A: QUANTIFICATIONS OF THE X-RAY DIFFRACTION RESULTS

The volume proportions between the strained and partially relaxed $LaCoO_3$ fractions on different substrates were estimated by performing fits to the θ-2θ scans, where the Voigt function is used as the model function of a feature. The fitting results are presented in Fig. 8. By comparing the ratio between the areas of the strained and partially relaxed features, we found that ∼73%(∼90%) of the $LaCoO_3$ film on $SrTiO_3(LaAlO_3)$ is fully strained, as indicated in Table II. Qualitatively, we conclude that the majority of the $LaCoO_3$ film is strained coherently on the $LaAlO_3$, whereas there is a

TABLE II. Quantifications of the x-ray diffraction results for the $LaCoO_3$ films. The intensity unit is given in the ratio percentage of the two components. The angle position and feature width are in degrees.

	On $LaAlO_3$		On $SrTiO_3$	
	Strained	Relaxed	Strained	Relaxed
Intensity	90 ± 1	10 ± 1	73 ± 10	27 ± 10
Position	47.28 ± 0.01	47.55 ± 0.01	47.96 ± 0.01	47.66 ± 0.01
Width	0.35 ± 0.01	0.15 ± 0.01	0.28 ± 0.01	0.52 ± 0.08

significant part which is partially relaxed for the film on the $SrTiO_3$.

APPENDIX B: SATURATION OF THE ELASTIC PEAK

The RIXS intensity near the zero loss region is lower in the experiments than in the calculations. A possible reason for this discrepancy is the energy-dependent self-absorption effect. The RIXS intensity is influenced by the absorption factor of the incident and the emitted photon. For a larger absorption factor, the spectra will be more saturated. Figure 9(a) shows the simulation of this state-dependent saturation effect. The zero energy line of the L_3 edge RIXS spectra has an emitted photon energy equal to the maximum of the L_3 edge, which shows the strongest intensity saturation due to self-absorption. In contrast, the high-energy-loss region features show less saturation effect. This also implies that normalizing to the fluorescence feature is a valid approach. Another reason for the discrepancy between the experimental data and the calculations can be that all the CoO_6 clusters are assumed to be well aligned to the pseudocubic orientation (002), which provides maximum dichroism intensity. Experimentally, not all the CoO_6 clusters will be aligned exactly to the pseudocubic orientation. For instance, the strain-induced rotational modifications observed by TEM will introduce some rotational variations. These rotational variations lead to the mixture of different polarization dependent effects, see Fig. 9(b).

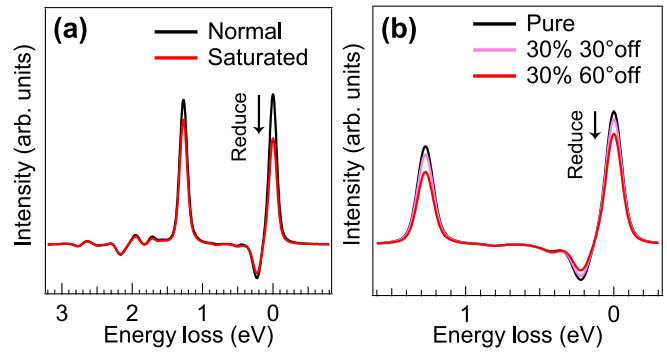

FIG. 9. The comparison of the simulated dichroism spectra (a) with considering the saturation and self-absorption effect and (b) with considering off-aligned fractions with an angle of 0° (pure), 30° (30%), and 60° (30%) from global z axis. The calculation is tested for the optimized case Ds $= -0.12$ eV.

[1] J.-Q. Yan, J. S. Zhou, and J. B. Goodenough, Phys. Rev. B **69**, 134409 (2004).

[2] M. Abbate, J. C. Fuggle, A. Fujimori, L. H. Tjeng, C. T. Chen, R. Potze, G. A. Sawatzky, H. Eisaki, and S. Uchida, Phys. Rev. B **47**, 16124 (1993).

[3] K. Asai, A. Yoneda, O. Yokokura, J. M. Tranquada, G. Shirane, and K. Kohn, J. Phys. Soc. Jpn. **67**, 290 (1998).

[4] A. Ishikawa, J. Nohara, and S. Sugai, Phys. Rev. Lett. **93**, 136401 (2004).

[5] Z. Ropka and R. J. Radwanski, Phys. Rev. B **67**, 172401 (2003).

[6] M. W. Haverkort, Z. Hu, J. C. Cezar, T. Burnus, H. Hartmann, M. Reuther, C. Zobel, T. Lorenz, A. Tanaka, N. B. Brookes, H. H. Hsieh, H.-J. Lin, C. T. Chen, and L. H. Tjeng, Phys. Rev. Lett. **97**, 176405 (2006).

[7] D. Fuchs, C. Pinta, T. Schwarz, P. Schweiss, P. Nagel, S. Schuppler, R. Schneider, M. Merz, G. Roth, and H. V. Löhneysen, Phys. Rev. B **75**, 144402 (2007).

[8] D. Fuchs, E. Arac, C. Pinta, S. Schuppler, R. Schneider, and H. v. Löhneysen, Phys. Rev. B **77**, 014434 (2008).

[9] J. Fujioka, Y. Yamasaki, H. Nakao, R. Kumai, Y. Murakami, M. Nakamura, M. Kawasaki, and Y. Tokura, Phys. Rev. Lett. **111**, 027206 (2013).

[10] J. Fujioka, Y. Yamasaki, A. Doi, H. Nakao, R. Kumai, Y. Murakami, M. Nakamura, M. Kawasaki, T. Arima, and Y. Tokura, Phys. Rev. B **92**, 195115 (2015).

[11] J. W. Freeland, J. X. Ma, and J. Shi, Appl. Phys. Lett. **93**, 212501 (2008).

[12] B. Rivas-murias, I. Lucas, and P. Jime, Nano Lett. **16**, 1736 (2016).

[13] D. Meng, H. Guo, Z. Cui, C. Ma, J. Zhao, J. Lu, H. Xu, Z. Wang, X. Hu, Z. Fu, R. Peng, J. Guo, X. Zhai, G. J. Brown, R. Knize, and Y. Lu, Proc. Nat. Acad. Sci. **115**, 2873 (2018).

[14] G. E. Sterbinsky, P. J. Ryan, J.-W. Kim, E. Karapetrova, J. X. Ma, J. Shi, and J. C. Woicik, Phys. Rev. B **85**, 020403(R) (2012).

[15] S. J. May, J.-W. Kim, J. M. Rondinelli, E. Karapetrova, N. A. Spaldin, A. Bhattacharya, and P. J. Ryan, Phys. Rev. B **82**, 014110 (2010).

[16] K. Gupta and P. Mahadevan, Phys. Rev. B **79**, 020406(R) (2009).

[17] H. Hsu, P. Blaha, and R. M. Wentzcovitch, Phys. Rev. B **85**, 140404(R) (2012).

[18] V. V. Mehta, N. Biskup, C. Jenkins, E. Arenholz, M. Varela, and Y. Suzuki, Phys. Rev. B **91**, 144418 (2015).

[19] A. O. Fumega and V. Pardo, Phys. Rev. Mater. **1**, 054403 (2017).

[20] M. Merz, P. Nagel, C. Pinta, A. Samartsev, H. V. Löhneysen, M. Wissinger, S. Uebe, A. Assmann, D. Fuchs, and S. Schuppler, Phys. Rev. B **82**, 174416 (2010).

[21] H. Zhang, J. Zhang, H. Yang, Q. Lan, D. Hong, S. Wang, X. Shen, T. Khan, R. Yu, J. Sun, and B. Shen, Appl. Mater. Interfaces **8**, 18328 (2016).

[22] L. Qiao, J. H. Jang, D. J. Singh, Z. Gai, H. Xiao, A. Mehta, R. K. Vasudevan, A. Tselev, Z. Feng, H. Zhou, S. Li, W. Prellier,

X. Zu, Z. Liu, A. Borisevich, A. P. Baddorf, and M. D. Biegalski, Nano Lett. **15**, 4677 (2015).

[23] W. S. Choi, J. H. Kwon, H. Jeen, J. E. Hamann-Borrero, A. Radi, S. Macke, R. Sutarto, F. He, G. A. Sawatzky, V. Hinkov, M. Kim, and H.-N. Lee, Nano Lett. **12**, 4966 (2012).

[24] J.-H. Kwon, W. S. Choi, Y.-K. Kwon, R. Jung, J.-M. Zuo, H. N. Lee, and M. Kim, Chem. Mater. **26**, 2496 (2014).

[25] N. Biškup, J. Salafranca, V. Mehta, M. P. Oxley, Y. Suzuki, S. J. Pennycook, S. T. Pantelides, and M. Varela, Phys. Rev. Lett. **112**, 087202 (2014).

[26] G. Ghiringhelli, A. Piazzalunga, C. Dallera, T. Schmitt, V. N. Strocov, J. Schlappa, L. Patthey, X. Wang, H. Berger, and M. Grioni, Phys. Rev. Lett. **102**, 027401 (2009).

[27] M. Moretti Sala, V. Bisogni, C. Aruta, G. Balestrino, H. Berger, N. B. Brookes, G. M. de Luca, D. Di. Castro, M. Grioni, M. Guarise, P. G. Medaglia, F. Miletto Granozio, M. Minola, P. Perna, M. Radovic, M. Salluzzo, T. Schmitt, K. J. Zhou, L. Braicovich, and G. Ghiringhelli, New J. Phys. **13**, 043026 (2011).

[28] M. Magnuson, S. M. Butorin, J.-H. Guo, and J. Nordgren, Phys. Rev. B **65**, 205106 (2002).

[29] S. G. Chiuzbăian, T. Schmitt, M. Matsubara, A. Kotani, G. Ghiringhelli, C. Dallera, A. Tagliaferri, L. Braicovich, V. Scagnoli, N. B. Brookes, U. Staub, and L. Patthey, Phys. Rev. B **78**, 245102 (2008).

[30] S. M. Butorin, J.-H. Guo, M. Magnuson, and J. Nordgren, Phys. Rev. B **55**, 4242 (1997).

[31] A. Agui, T. Uozumi, M. Mizumaki, and T. Käämbre, Phys. Rev. B **79**, 092402 (2009).

[32] G. Fabbris, D. Meyers, J. Okamoto, J. Pelliciari, A. S. Disa, Y. Huang, Z.-Y. Chen, W. B. Wu, C. T. Chen, S. Ismail-Beigi, C. H. Ahn, F. J. Walker, D. J. Huang, T. Schmitt, and M. P. M. Dean, Phys. Rev. Lett. **117**, 147401 (2016).

[33] R.-P. Wang, B. Liu, R. J. Green, M. U. Delgado-Jaime, M. Ghiasi, T. Schmitt, M. M. van Schooneveld, and F. M. F. de Groot, J. Phys. Chem. C **121**, 24919 (2017).

[34] M. M. van Schooneveld, R. Kurian, K. Zhou, J. Schlappa, V. N. Strocov, T. Schmitt, and F. M. F. de Groot, J. Phys. Chem. C **116**, 15218 (2012).

[35] J. Schlappa, T. Schmitt, F. Vernay, V. N. Strocov, V. Ilakovac, B. Thielemann, H. M. Rønnow, S. Vanishri, A. Piazzalunga, X. Wang, L. Braicovich, G. Ghiringhelli, C. Marin, J. Mesot, B. Delley, and L. Patthey, Phys. Rev. Lett. **103**, 047401 (2009).

[36] L. Braicovich, L. J. P. Ament, V. Bisogni, F. Forte, C. Aruta, G. Balestrino, N. B. Brookes, G. M. De Luca, P. G. Medaglia, F. Miletto Granozio, M. Radovic, M. Salluzzo, J. van den Brink, and G. Ghiringhelli, Phys. Rev. Lett. **102**, 167401 (2009).

[37] L. Braicovich, J. van den Brink, V. Bisogni, M. M. Sala, L. J. P. Ament, N. B. Brookes, G. M. De Luca, M. Salluzzo, T. Schmitt, V. N. Strocov, and G. Ghiringhelli, Phys. Rev. Lett. **104**, 077002 (2010).

[38] H. Y. Huang, C. J. Jia, Z. Y. Chen, K. Wohlfeld, B. Moritz, T. P. Devereaux, W. B. Wu, J. Okamoto, W. S. Lee, M. Hashimoto, Y. He, Z. X. Shen, Y. Yoshida, H. Eisaki, C. Y. Mou, C. T. Chen, and D. J. Huang, Sci. Rep. **6**, 19657 (2016).

[39] G. Fabbris, D. Meyers, L. Xu, V. M. Katukuri, L. Hozoi, X. Liu, Z.-Y. Chen, J. Okamoto, T. Schmitt, A. Uldry, B. Delley, G. D. Gu, D. Prabhakaran, A. T. Boothroyd, J. van den Brink, D. J. Huang, and M. P. M. Dean, Phys. Rev. Lett. **118**, 156402 (2017).

[40] A. Pietzsch, F. Hennies, P. S. Miedema, B. Kennedy, J. Schlappa, T. Schmitt, V. N. Strocov, and A. Föhlisch, Phys. Rev. Lett. **114**, 088302 (2015).

[41] S. Moser, S. Fatale, P. Krüger, H. Berger, P. Bugnon, A. Magrez, H. Niwa, J. Miyawaki, Y. Harada, and M. Grioni, Phys. Rev. Lett. **115**, 096404 (2015).

[42] R.-P. Wang, A. Hariki, A. Sotnikov, F. Frati, J. Okamoto, H.-Y. Huang, A. Singh, D.-J. Huang, K. Tomiyasu, C.-H. Du, J. Kuneš, and F. M. F. de Groot, Phys. Rev. B **98**, 035149 (2018).

[43] H. Y. Huang, Z. Y. Chen, R.-P. Wang, F. M. F. de Groot, W. B. Wu, J. Okamoto, A. Chainani, A. Singh, Z.-Y. Li, J. S. Zhou, H. T. Jeng, J. G. Guo, G. Y.and Park, L. H. Tjeng, C. T. Chen, and D. J. Huang, Nat. Commun. **8**, 15929 (2017).

[44] B. Liu, R.-P. Wang, E. N. Glass, C. L. Hill, T. Cuk, J. Okamoto, D. J. Huang, M. M. van Schooneveld, and F. M. F. de Groot, Inorg. Chem. **55**, 10152 (2016).

[45] Y. Yokoyama, Y. Yamasaki, M. Taguchi, Y. Hirata, K. Takubo, J. Miyawaki, Y. Harada, D. Asakura, J. Fujioka, M. Nakamura, H. Daimon, M. Kawasaki, Y. Tokura, and H. Wadati, Phys. Rev. Lett. **120**, 206402 (2018).

[46] K. Tomiyasu, J. Okamoto, H. Y. Huang, Z. Y. Chen, E. P. Sinaga, W. B. Wu, Y. Y. Chu, A. Singh, R.-P. Wang, F. M. F. de Groot, A. Chainani, S. Ishihara, C. T. Chen, and D. J. Huang, Phys. Rev. Lett. **119**, 196402 (2017).

[47] A. Harada, T. Taniyama, Y. Takeuchi, T. Sato, T. Kyômen, and M. Itoh, Phys. Rev. B **75**, 184426 (2007).

[48] H. Gercek, Int. J. Rock Mech. Min. Sci. **44**, 1 (2007).

[49] A. Herklotz, A. D. Rata, L. Schultz, and K. Dörr, Phys. Rev. B **79**, 092409 (2009).

[50] A. D. Rata, A. Herklotz, L. Schultz, and K. Dörr, Eur. Phys. J. B **76**, 215 (2010).

[51] F. M. F. de Groot, Coord. Chem. Rev. **249**, 31 (2005).

[52] A. Uldry, F. Vernay, and B. Delley, Phys. Rev. B **85**, 125133 (2012).

[53] M. W. Haverkort, M. Zwierzycki, and O. K. Andersen, Phys. Rev. B **85**, 165113 (2012).

[54] P. W. Anderson, Phys. Rev. **124**, 41 (1961).

[55] C. H. Lai, H. S. Fung, W. B. Wu, H. Y. Huang, H. W. Fu, S. W. Lin, S. W. Huang, C. C. Chiu, D. J. Wang, L. J. Huang, T. C. Tseng, S. C. Chung, C. T. Chen, and D. J. Huang, J. Synchrotron Rad. **21**, 325 (2014).

[56] H. S. Fung, C. T. Chen, L. J. Huang, C. H. Chang, S. C. Chung, D. J. Wang, T. C. Tseng, and K. L. Tsang, in *Eighth International Conference on Synchrotron Radiation Instrumentation*, edited by T. Warwick, J. Stöhr, H. A. Padmore, and J. Arthur, AIP Conf. Proc. No. 705 (AIP, New York, 2004), p. 655.

[57] Y. Kobayashi, T. S. Naing, M. Suzuki, M. Akimitsu, K. Asai, K. Yamada, J. Akimitsu, P. Manuel, J. M. Tranquada, and G. Shirane, Phys. Rev. B **72**, 174405 (2005).

[58] H. Gretarsson, J. P. Clancy, Y. Singh, P. Gegenwart, J. P. Hill, J. Kim, M. H. Upton, A. H. Said, D. Casa, T. Gog, and Y.-J. Kim, Phys. Rev. B **87**, 220407(R) (2013).

[59] G. E. Sterbinsky, R. Nanguneri, J. X. Ma, J. Shi, E. Karapetrova, J. C. Woicik, H. Park, J.-W. Kim, and P. J. Ryan, Phys. Rev. Lett. **120**, 197201 (2018).